Advances in Computational Science and Engineering

doi:10.3934/acse.2023013

ISOGEOMETRIC SIMULATION OF A DERIVED STEM CELL ENGINEERED VENTRICLE

Sofia Botti[1,2] and Michele Torre[3]*

[1]Department of Mathematics, University of Pavia, Italy

[2]Euler Insitute, Università della Svizzera Italiana, Switzerland

[3]Department of Civil Engineering and Architecture, University of Pavia, Italy

(Communicated by Antonia Larese)

Abstract. Regenerative cardiology recently advanced in patient-specific medicine by employing somatic cells to derive pluripotent stem cells and differentiate them into cardiomyocytes.

In this work, the cardiac *Monodomain* model is coupled with stem cell ionic models to simulate the action potential propagation in the engineered ventricle. The cardiac model is then discretized by means of Isogeometric Analysis, carrying out numerical experiments to assess the accuracy of the approach. Finally, the presented framework is used to investigate the propagation of an action potential on the calibrated model of the engineered ventricle.

1. **Introduction.** Human Induced Pluripotent Stem Cells-Derived Cardiomyocytes (hiPSC-CMs) are spontaneously beating cardiomyocytes derived from somatic cells. This field was pioneered in 2006 by S. Yamanaka [27], who was awarded the Nobel Prize in Medicine in 2012 for the discovery of mature cells reprogrammed to become pluripotent and driven toward the cardiac lineage through differentiation protocols [26]. hiPSC-CMs express the major cardiac markers and ion channels, they are functionally like adult human cardiomyocytes, and exhibit expected responses to cardiac stimuli. Although several studies have shown that hiPSC-CMs have molecular, structural, and functional properties resembling those of adult cardiomyocytes, they have proved to be less mature than adult cells, as they do not display the sub-cellular, cellular and tissue-level adult myocyte morphology and sarcomeric protein content and organization [17]. Even though such cells are molecularly and functionally immature, in the cardiovascular field, hiPSC-CMs provide a powerful tool to develop reliable *in-vitro* models for drug toxicity screening.

The possibility to engineer hiPSC-derived cardiac cell cultures being as similar as possible to undiseased and diseased regions of the human heart is the first step to improving the translation of hiPSC-CMs to humans. 2D cultures of hiPSC-CMs are often used as a platform for investigating new therapies, even if intrinsic limitations arise in terms of spatial architecture. Re-creating *in-vitro* a reliable 3D

2020 *Mathematics Subject Classification.* Primary: 65D07, 65M99; Secondary: 65Z05.

Key words and phrases. Isogeometric analysis, cardiac electrophysiology, computational cardiology, derived stem cardiomyocytes, engineered ventricle.

*Corresponding author: Michele Torre.

tissue is undoubtedly more complex than using standard cell cultures, and several new aspects have to be considered simultaneously. Besides these efforts, researchers have bioengineered a three-dimensional model of a human left heart ventricle, used to measure time-dependent pressure and volume, as described in [19, 18].

Since modern cardiac models have transformed and increased the understanding of cardiac function in health and disease and the clinical practice of cardiology [30], a virtual rendering of the engineered ventricle can provide a robust environment to conduct preliminary investigations, otherwise entailing expensive trial-and-error tests. In this direction, this work aims to develop a comprehensive framework, based on Isogeometric Analysis, for electrophysiological simulations representing the response of engineered tissues. The mathematical modeling of the heart involves systems of partial differential equations (PDEs) and ordinary differential equations (ODEs) coupled to model cardiac electrophysiology.

To describe the proposed model, we start, in Section 2, with the description of the ventricle architecture and we review the micro and macroscopic models of cardiac electrophysiology at the continuous level. In Section 3, we introduce the numerical methods to discretize the space, by means of Isogeometric Analysis, and time. Section 4 provides an extensive analysis of the method accuracy varying the spatial discretization, that aims to select the scheme for an effective simulation. Afterward, we calibrate the model and reproduce the propagation of the action potential in the engineered ventricle. Finally, Section 5 recapitulates the main findings and derives possible future perspectives.

2. **Biophysical model of the engineered ventricle.**

In the following section, we briefly present the tissue-engineered scale model of the ventricle, which we model using an isogeometric approach. Firstly, we describe the geometry of the *in-vitro* model and the formulation adopted for the modeling of hiPSC-CMs. Afterward, we describe the *Monodomain* formulation, entailing a reaction-diffusion PDE coupled with a suitable ionic model, employed to model the tissue. Finally, we present the splitting of the reactive and diffusive terms of the PDE by means of continuous Strang operator, posing the base for the numerical discretization.

2.1. **hiPSC-CMs ventricle model.**

By *Engineered heart tissue* we mean three-dimensional muscle strips, or muscular thin films, that can be generated from isolated heart cells or hiPSC-CMs [7, 31, 9]. Herein, we are taking into account the tissue-engineered scale model built at Harvard University [19, 18], where the scaffold was designed taking inspiration from the human myocardial tissue architecture and recreated using a nanofiber production system. The strategy developed for the production of a nanofiber ventricle is based on pull-spinning fibers on a rotating ellipsoidal collector. The resulting fabricated thin-wall chambers were then sutured to tubing or bioreactor components. Catheter sensors were then introduced and stable contraction of hiPSC-CM ventricles permitted time-dependent pressure and volume measurements. Thus, this kind of scaffold can promote the assembly of cardiomyocytes into functional 3D tissue-engineered ventricle chambers.

In order to model this engineered ventricular chamber, we use the ellipsoidal geometry of the scaffold presented in [19] and depicted in Figure 1. Indeed, the engineered ventricle manufacturing process consists of seeding and growing hiPSC-CMs on a scaffold previously formed on a collector. We schematize such a shape using a constant-thickness extrusion of the molding surface, even though it becomes irregular during cell maturation.

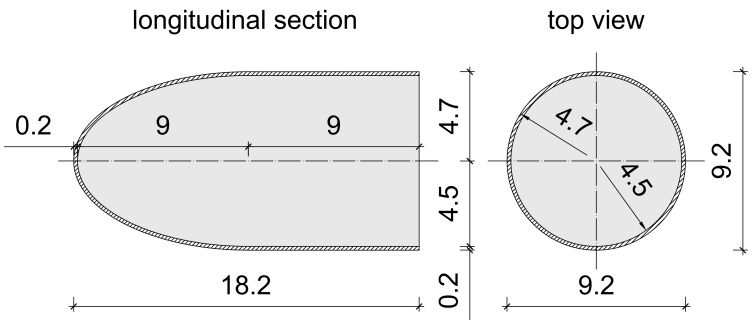

FIGURE 1. Schematic representation of the ellipsoidal scaffold. Dimensions are expressed in millimeters.

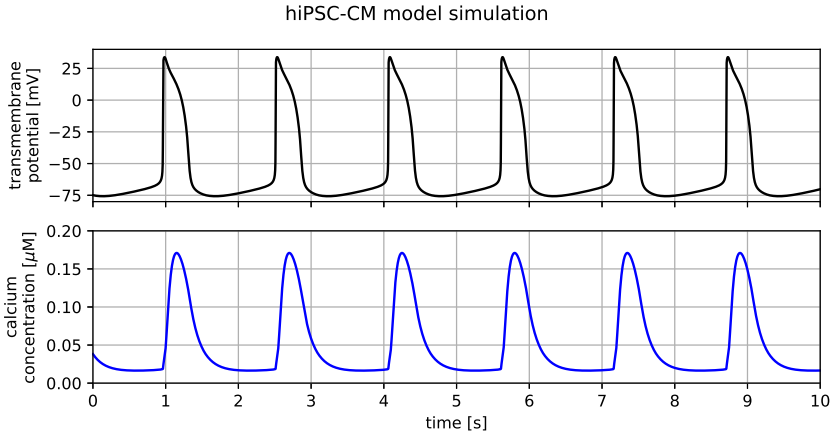

FIGURE 2. The adopted ionic model. Ten seconds of simulations show the spontaneous firing activity of the transmembrane potential v (top), and Ca^{2+} concentration in the sarcoplasmic reticulum (bottom).

2.2. **The ionic model for cells at the microscale.** Cardiomyocyte cultures include spontaneously beating cells, but also express a mixture of different adult profiles, such as atrial, ventricular, and nodal markers [15]. Because of these significant differences with respect to adult myocytes, models of adult cardiac action potential inadequately describe the hiPSC-CM electrophysiology. To fill this gap, some specific computational methods have been developed in the last decade. A primal formulation was published in 2013 [21], then updated in 2018 with a more flexible Calcium (Ca^{2+}) handling formulation, [22]. This model focused on the ventricular-like phenotype, the predominant phenotype emerging during the differentiation process. A deep analysis of different ionic models for hiPSC-CMs has been conducted in [4].

The latter ionic model is perfectly suitable to model an engineered tissue, since it recapitulates several relevant features of hiPSC-CMs, such as the Ca^{2+} concentration and the spontaneous firing activity, shown in Figure 2. Consequently, we adopt such a model [22] to simulate the electrophysiological activity of the tissue.

The ionic model describes the evolution in time of the transmembrane potential and several ionic currents following the classical Hodgkin-Huxley formulation. For a detailed presentation of the equations underlying the model, the reader is referred to [22]. Herein, we sum up some relevant features. The system of ODEs consists in a set of 22 variables, differentiated into *(i)* the transmembrane potential v; *(ii)* 3 ionic concentrations c^s (Na_i, Ca_i, Ca_{SR}); *(iii)* 15 gating variables w^r, involved in 7 different membrane currents; *(iv)* 3 gating variables w^r (RyR_o, RyR_c, RyR_a), standing for the Ryanodine Receptors' probabilities of activation, inactivation and adaptation, needed for the novel characterization of Ca^{2+} dynamic, [13]. Such an ionic model is integrated in the tissue formulation through equations (2c), (2d), and (2e).

2.3. **The *Monodomain* formulation for tissues at the macroscale.** The canonical description of cardiac electrophysiology models the behaviour of the tissue in space ($\boldsymbol{x} \in \Omega$) and time ($t \in (0,T)$) by means of two superimposed continua, representing the intra-cellular and the extra-cellular spaces. These compartments exchange the charge via the ionic current I^{ion} across the cellular membrane, whose intensity depends in a point-wise manner *(i)* on the difference between the intra-cellular potential u_i and the extra-cellular potential u_e

$$v(\boldsymbol{x},t) = u_i(\boldsymbol{x},t) - u_e(\boldsymbol{x},t), \tag{1}$$

and *(ii)* on the cellular state by means of the s ion concentrations c^s and the r gating variables w^r. Inside a single compartment, the charge redistributes according to the linear diffusion law governed by the conductivity tensors $\mathbf{D}$, $\mathbf{D}_e$, for the intra-cellular and extra-cellular spaces respectively, linking the local cellular state to the one of the neighboring cells.

Moreover, the charge flux through the cellular membrane depends on the capacitance C_m and ratio χ – between the membrane surface area and the volume enclosed by this surface – regulating the time delay, while intra-cellular I_i^{app} and extra-cellular I_e^{app} currents can be applied to simulate external stimuli. The charge conservation law finally leads to the *Bidomain* formulation [25, 8, 11]. It embeds the single-cell model, described by a system of ODEs (equations (2c), (2d), and (2e)), into the tissue model (PDEs (2a) and (2b)):

$$\begin{cases} \chi C_m \dfrac{\partial v}{\partial t} - \nabla\cdot(\mathbf{D}\nabla v) - \nabla\cdot(\mathbf{D}\nabla u_e) + \chi I^{ion} = I_i^{app} & \text{in } \Omega\setminus\partial\Omega\times(0,T) \quad (2a)\\ -\nabla\cdot(\mathbf{D}\nabla v) - \nabla\cdot((\mathbf{D}+\mathbf{D}_e)\nabla u_e) = I_e^{app} + I_i^{app} & \text{in } \Omega\setminus\partial\Omega\times(0,T) \quad (2b)\\ I^{ion} = I^{ion}\left(v, w^1, \dots, w^{18}, c^1, c^2, c^3\right) & \text{in } \Omega\times(0,T) \quad (2c)\\ \dfrac{\partial w^r(\boldsymbol{x},t)}{\partial t} = m_w^r\left(v, w^1, \dots, w^{18}\right) \text{ for } r = 1,\dots,18 & \text{in } \Omega\times(0,T) \quad (2d)\\ \dfrac{\partial c^s(\boldsymbol{x},t)}{\partial t} = m_c^s\left(v, w^1, \dots, w^{18}, c^1, c^2, c^3\right) \text{ for } s = 1,2,3 & \text{in } \Omega\times(0,T). \quad (2e) \end{cases}$$

The system is then coupled with appropriate initial conditions for both transmembrane potential and ionic model variables

$$\begin{cases} v(\boldsymbol{x},0) = v_0 & \text{(3a)} \\ w^r(\boldsymbol{x},0) = w_0^r \quad \text{for } r = 1,\dots,18 & \text{(3b)} \\ c^s(\boldsymbol{x},0) = c_0^s \quad \text{for } s = 1,2,3. & \text{(3c)} \end{cases}$$

and homogeneous Neumann boundary conditions for the no flux assumption through the external surface $\partial\Omega$ (i.e., we suppose an electrically isolated domain):

$$\begin{cases} \mathbf{n}\cdot\mathbf{D}\nabla\left(v+u_e\right) = 0 & \text{on } \partial\Omega\times(0,T) & \text{(4a)} \\ \mathbf{n}\cdot\left(\mathbf{D}+\mathbf{D}_e\right)\nabla u_e + \mathbf{n}\cdot\mathbf{D}\nabla v = 0 & \text{on } \partial\Omega\times(0,T) & \text{(4b)} \end{cases}$$

where $\mathbf{n}$ is the outward pointing normal. Dirichlet boundary conditions can be included as presented in [8]. Finally, since the charge has to be conserved, the applied currents have to obey to the compatibility condition:

$$\int_\Omega \left(I_i^{app} + I_e^{app}\right) d\boldsymbol{x} = 0. \tag{5}$$

The conductivity of an engineered tissue built on a scaffold depends on *(i)* the spatial organization and geometrical orientation of the cells [14], and *(ii)* on the gap junctions expression and other biological factors related to the cell maturation [19, 18]. The engineered ventricle manufacturing process guarantees a high cell alignment, quantified by the Oriental Order Parameter, in the circumferential direction. Coherently, we assume an anisotropic, transversally isotropic, intercellular conductivity tensor with a greater eigenvalue in the fiber direction. The cell maturation affects the conductivity in an involved manner, resulting in a complex experimental quantification of the parameters. We simplify the mathematical formulation by assuming that the extracellular and intercellular conductivity are proportional:

$$\mathbf{D}_e = \lambda\mathbf{D}, \tag{6}$$

as already done in patient-specific simulations of the human heart [16] and in analysis of the cardiac tissue [23, 5]. Consequently, we reduce the number of unknown parameters to two: the intra-cellular conductivity in the direction of the fibers and in the orthogonal direction, which we can calibrate using the available experimental results.

The equal anisotropy hypothesis (equation (6)) greatly simplifies the Bidomain formulation (equations (2a), (2b), and (4)). Indeed, after some algebraic manipulations, presented in [25], we recover the *Monodomain* formulation:

$$\begin{cases} \dfrac{\partial v}{\partial t} = -\dfrac{1}{C_m} I^{ion} + \dfrac{1}{\chi C_m\left(\lambda+1\right)}\left[\lambda\nabla\cdot\left(\mathbf{D}\nabla v\right) + \left(\lambda I_i^{app} - I_e^{app}\right)\right] \\ \qquad\qquad\qquad\qquad\qquad\qquad\qquad\qquad \text{in} \quad \Omega\setminus\partial\Omega\times(0,T) \\ \mathbf{n}\cdot\mathbf{D}\nabla v = 0 \qquad\qquad\qquad\qquad\qquad\qquad \text{on} \quad \partial\Omega\times(0,T)\,, \end{cases} \tag{7}$$

that describes the electrophysiology of the tissue with a single PDE coupled to (2c), (2d), and (2e). Clearly, the *Monodomain* formulation is less demanding from the computational point of view, leading to better-conditioned matrices in the discrete approximation.

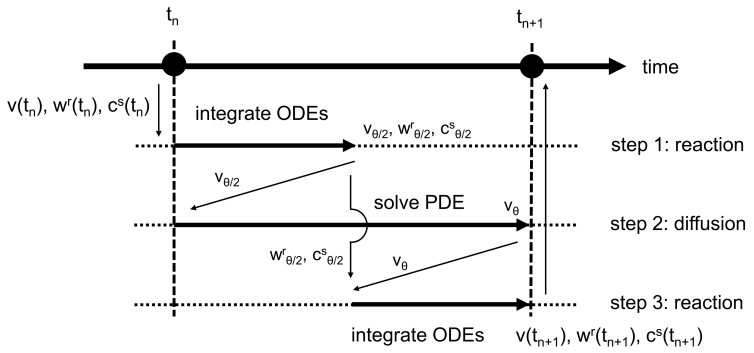

FIGURE 3. Schematic representation of the Strang splitting operator.

2.4. **Strang operator splitting.** To solve the *Monodomain* formulation in equation (7), we adopt the Strang's symmetrical splitting scheme [25], which is a second-order accurate operator. This fractional step method separates the integration in time of the diffusive and reactive terms [23, 24] subdividing the solution process in an arbitrary time interval ($t \in [t_n, t_{n+1}]$) in three steps as schematized in Figure 3.

Step 1. Given the initial conditions $v(t_n)$, $w^r(t_n)$, and $c^s(t_n)$ we integrate the reactive term (i.e., the ionic model) to find v, w^r, and c^s at time $t_{\theta/2}$, being $\theta/2$ the midpoint of the time interval. The integration of the system:

$$\begin{cases} \dfrac{\partial v}{\partial t} = -\dfrac{1}{C_m} I^{ion}\left(v, w^1, \ldots, w^{18}, c^1, c^2, c^3\right) & \forall t \in \left[t_n, t_{\theta/2}\right] \quad (8a) \\ \dfrac{\partial w^r}{\partial t} = m_w^r\left(v, w^1, \ldots, w^{18}\right) \quad \text{for } r = 1, \ldots, 18 & \forall t \in \left[t_n, t_{\theta/2}\right] \quad (8b) \\ \dfrac{\partial c^s}{\partial t} = m_c^s\left(v, w^1, \ldots, w^{18}, c^1, c^2, c^3\right) \quad \text{for } s = 1, 2, 3 & \forall t \in \left[t_n, t_{\theta/2}\right] \quad (8c) \end{cases}$$

returns $v_{\theta/2}, w^r_{\theta/2}, c^s_{\theta/2}$.

Step 2. Given the initial condition $v_{\theta/2}$, we integrate the diffusive term by solving the PDE:

$$\begin{cases} \dfrac{\partial v}{\partial t} = -\dfrac{1}{\chi C_m\left(\lambda+1\right)}\left[\lambda \nabla \cdot (\mathbf{D}\nabla v) + (\lambda I_i^{app} - I_e^{app})\right] & \text{in } \Omega,\ \forall t \in [t_n, t_{n+1}] \quad (9a) \\ \mathbf{n} \cdot \mathbf{D}\nabla v = 0 & \text{on } \partial\Omega,\ \forall t \in [t_n, t_{n+1}] \quad (9b) \end{cases}$$

to compute v_θ.

Step 3. Given as initial conditions $v_\theta, w^r_{\theta/2}, c^s_{\theta/2}$, we integrate the reactive term for $t \in \left[t_{\theta/2}, t_{n+1}\right]$ and the system

$$\begin{cases} \dfrac{\partial v}{\partial t} = -\dfrac{1}{C_m} I^{ion}\left(v, w^1, \ldots, w^{18}, c^1, c^2, c^3\right) & \forall t \in \left[t_{\theta/2}, t_{n+1}\right] \quad (10a) \\ \dfrac{\partial w^r}{\partial t} = m_w^r\left(v, w^1, \ldots, w^{18}\right) \quad \text{for } r = 1, \ldots, 18 & \forall t \in \left[t_{\theta/2}, t_{n+1}\right] \quad (10b) \\ \dfrac{\partial c^s}{\partial t} = m_c^s\left(v, w^1, \ldots, w^k, c^1, c^2, c^3\right) \quad \text{for } s = 1, 2, 3 & \forall t \in \left[t_{\theta/2}, t_{n+1}\right] \quad (10c) \end{cases}$$

gives as a result $v(t_{n+1}), w^r(t_{n+1}), c^s(t_{n+1})$.

We remark that the operator does not discretize in time the equations, as highlighted in [25]. Indeed, the time integration schemes will be introduced in the following.

3. Isogeometric framework and discrete problem.

Isogeometric Analysis (IGA) is the framework for the spatial approximation of PDEs herein adopted, which uses spline functions for the geometrical representation of the computational domain and the approximation of the unknown fields. Thus, the geometrical mapping described in Section 3.2 defines the basis functions used in the computation of the transmembrane potential and its derivatives.

3.1. B-spline functions for approximations.

In the present work, we test several shape functions to assess the effect of the polynomial degree and continuity at the element interfaces on the numerical approximation of potential. We focus on multi-variate B-splines basis functions, defined through the tensor product of uni-variate B-splines, as they easily control these features. Indeed, the degree p and the open knot vector $\Xi = \left\{\xi_1, \xi_2, \dots, \xi_{m_\xi+p+1}\right\}$ define the m_ξ splines $\mathrm{H}_a(\xi)$ in the parametric direction ξ through the Cox-de Boor recursive formula:

$$\text{for } p = 0 \quad \mathrm{H}_{a;0}(\xi) = \begin{cases} 1 & \text{if } \xi_\mathrm{a} \le \xi < \xi_{\mathrm{a}+1} \\ 0 & \text{otherwise} \end{cases}$$

$$\text{for } p = 1, 2, 3, \dots \quad \mathrm{H}_{\mathrm{a};p}(\xi) = \frac{\xi - \xi_\mathrm{a}}{\xi_{\mathrm{a}+p} - \xi_\mathrm{a}} \mathrm{H}_{a;p-1}(\xi) + \frac{\xi_{\mathrm{a}+p+1} - \xi}{\xi_{\mathrm{a}+p+1} - \xi_{\mathrm{a}+1}} \mathrm{H}_{\mathrm{a}+1;p-1}(\xi). \tag{11}$$

By increasing the multiplicity of a knot of the vector Ξ, we reduce the spline continuity at that element interface.

To define functions in a 3D space, we take the tensor product of uni-variate B-splines H, L, and K in three different parametric directions ξ, η, ζ, for which similar definitions hold. Moreover, assuming a lexicographical order, we recast such functions in the vector $\mathbf{N}$ as follows:

$$\mathrm{N}_a = \mathrm{H}_b(\xi)\,\mathrm{L}_c(\eta)\,\mathrm{K}_d(\zeta). \tag{12}$$

Following the standard isogeometric approach, we define the geometry of the body as a linear combination of basis functions and control points – also referred as nodes – coordinates $\mathbf{B}_a$ as follows:

$$\boldsymbol{x}(\xi, \eta, \zeta) = \sum_{a=1}^{m} \mathrm{N}_a(\xi, \eta, \zeta)\,\mathbf{B}_a, \tag{13}$$

where m is the number of three-variate splines: $m = m_\xi \times m_\eta \times m_\zeta$.

In this work, we test three sets of splines to approximate v:

- degree $p = 1$ and continuity C^0, equivalent to linear hexahedral finite elements.
- high order splines with C^0 continuity, also known as Bernstein polynomials, obtained repeating the internal knots p times.
- high order splines with maximum continuity C^{p-1}, obtained using internal knots with multiplicity equal to one.

The accuracy of the basis functions is investigated in Section 4.1.

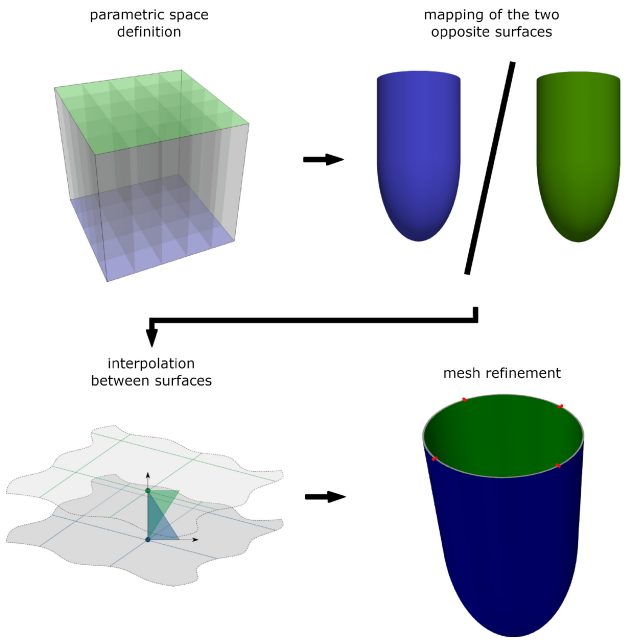

FIGURE 4. Schematic representation of the workflow to define the geometrical mapping. The 8 red dots (4 on the external and 4 on the internal surfaces) highlight the locations of the singularities of the geometrical mapping.

3.2. **Computation of the geometrical mapping.** In this work, we represent the ventricle as an extrusion between two opposite target surfaces mapped through the strategy herein presented and depicted in Figure 4.

The pipeline to define a structured mesh composed of hexahedral elements is similar to the one presented in [5], and it is articulated in four steps as follows.

Step 1. Initially, we set up the parametric space (i.e., we define the degree and knot vectors) to be mapped into the ventricle. We use a single three-variate patch to represent the ventricle selecting two opposite faces of the cube – for instance, the planes spanned by ξ and η at $\zeta = 0$ and $\zeta = 1$ – as the parent surfaces mapped into internal and external surfaces, in Figure 4 represented in green and blue, respectively. Coherently, the third parametric direction ζ refers to the transmural direction of the ventricle. We initially use a single linear element in such a direction to mimic the extrusion.

Step 2. The second step consists in mapping the two parametric surfaces (indexes $\bar{\zeta} \in 0, 1$) into the two main physical surfaces (indexes $j \in \{int, ext\}$) one at a time. Each surface is represented as:

$$\boldsymbol{x}^{*,j}\left(\xi,\eta,\bar{\zeta}\right) = \sum_{s=1}^{m_\xi \times m_\eta} \mathrm{N}_s\left(\xi,\eta,\bar{\zeta}\right) \mathbf{B}_s^{*,j} \tag{14}$$

where $\mathbf{B}_s^{*,j}$ are the coordinates of the control points related to the splines with support on the parametric surface (i.e., half of the set of splines). We optimize the control point coordinates such that the distance between the analytical surface $\boldsymbol{x}^{a,j}$ and its B-spline approximation $\boldsymbol{x}^{*,j}$ is minimized.

Such a problem is formalized as follows:

$$\mathbf{B}^{*,j} = \arg\min_{\mathbf{B}^{*,j}} \left\{ \| \boldsymbol{x}^{a,j} - \boldsymbol{x}^{*,j}\left(\mathbf{B}^{*,j}\right) \|^2 \right\}, \tag{15}$$

where we consider the standard L^2 norm as the metric for the computation of the distance between the surfaces sampled in a discrete set of points. Since the system is overdetermined, we solve equation (15) by means of least square method. In our simulation, we use equidistant points to sample the physical geometry and the parametric space.

In this application, the center of the selected face of the single-patch parametric space is mapped into the ventricle apex, whereas the edges correspond to the circular base. This strategy enables the mapping of the 3D engineered ventricle avoiding mapping singularities near the ventricle apex, which was the region of interest in the experimental investigation. However, it comes at a cost of eight singularities – corresponding to the vertex of the parametric cube – located at the ventricle base, as shown in Figure 4. Nevertheless, according to [12], they do not affect significantly the accuracy of the analysis because no Gauss point lies in those positions. If the surface under consideration is more complex, an alternative strategy is provided in Appendix A.

Step 3. Once the surfaces are mapped, we extrude the volume in direction ζ interpolating the two sets of coordinates $\mathbf{B}^{*,j}, j \in \{int, ext\}$ with a single linear element. Indeed, a one-to-one relation holds between the control points on opposite surfaces thanks to the tensor product structure of the parametric space.

Step 4. In the last step, the mesh is refined by employing the order elevation and knot insertion algorithms to achieve a suitable discretization for accurate simulations. For more details on the refinement scheme, the reader is referred to [6]. We remark that in this work we adopt the same polynomial degree in all the parametric directions, even in the transmural direction.

3.3. **Spatial discretization.** To discretize the *Monodomain* formulation, we consider the weak formulation of the PDE (7) defining the trial space for the transmembrane potential as

$$\mathcal{V} = \left\{ v | v \in H^1\left(\Omega, [0,T]\right) \right\}, \tag{16}$$

and assuming the test space $\delta\mathcal{V}$ equivalent to $\mathcal{V}$. In the previous definition, $H^1\left(\Omega, [0,T]\right)$ is the Sobolev space of functions with square integrable first derivatives in Ω. If Dirichlet boundary conditions are applied on $\partial\Omega_D$ and Neumann boundary conditions are applied on $\partial\Omega_N$, the formulation has to be modified as in [8] ($\partial\Omega_N \cup \partial\Omega_D = \partial\Omega$ and $\partial\Omega_N \cap \partial\Omega_D = \emptyset$). Moreover, we assume the gating variable w^r, the ionic concentration c^s, and their virtual variations (δw^r and δc^s) in

$$\mathcal{WC} = \left\{ f | f \in L^2\left(\Omega, [0,T]\right) \right\}, \tag{17}$$

where $L^2\left(\Omega, [0,T]\right)$ is the space of square integrable functions in Ω.

Then, the weak form of the *Monodomain* formulation combined with the Strang splitting scheme reads as follows [8]: $\forall t \in [0,T]$, find $v(t) \in \mathcal{V}, w^r(t), c^s(t) \in \mathcal{WC}$

such that the following relations hold for the first and the third steps of the splitting:

$$\begin{cases} \displaystyle\int_\Omega \delta v \frac{\partial v}{\partial t}\, d\boldsymbol{x} = -\frac{1}{C_m}\int_\Omega \delta v\, I^{ion}\, d\boldsymbol{x} & \forall \delta v \in \delta\mathcal{V} \quad (18a) \\ \displaystyle\int_\Omega \delta w \frac{\partial w^r}{\partial t}\, d\boldsymbol{x} = \int_\Omega \delta w\, m_w^r\, d\boldsymbol{x} & \forall \delta w \in \mathcal{WC}, r = 1,\dots,18 \quad (18b) \\ \displaystyle\int_\Omega \delta c \frac{\partial c^s}{\partial t}\, d\boldsymbol{x} = \int_\Omega \delta c\, m_c^s\, d\boldsymbol{x} & \forall \delta c \in \mathcal{WC}, s = 1,2,3 \quad (18c) \end{cases}$$

and the following equation holds for the second step (9a): $\forall \delta v \in \delta\mathcal{V}$

$$\int_\Omega \delta v \frac{\partial v}{\partial t}\, d\boldsymbol{x} = -\frac{1}{\chi C_m\,(\lambda+1)}\left(\int_\Omega \lambda \nabla \delta v \cdot \mathbf{D}\nabla v\, d\boldsymbol{x} + \int_\Omega \delta v\,(\lambda I_i^{app} - I_e^{app})\, d\boldsymbol{x}\right). \quad (19)$$

Replacing the functional spaces with a finite-dimensional approximation, the transmembrane potential v and the test functions δv are written as a linear combination of shape functions $\mathbf{N}$ – derived from the geometrical representation following the isoparametric paradigm – and control variables (i.e., the equivalent of the nodal values in the finite element method) $\hat{\mathbf{v}}$ and $\boldsymbol{\delta}\hat{\mathbf{v}}$ as

$$v(\boldsymbol{x},t) = \mathbf{N}(\boldsymbol{x})\,\hat{\mathbf{v}}(t) \quad (20)$$

$$\delta v(\boldsymbol{x},t) = \mathbf{N}(\boldsymbol{x})\,\boldsymbol{\delta}\hat{\mathbf{v}}(t). \quad (21)$$

In the present work, we test several shape functions to assess the accuracy of the discretizations. Therefore, the symbol $\mathbf{N}(\boldsymbol{x})$ refers to one of the generic sets of adopted basis functions.

By replacing equations (20) and (21) in (19), we obtain the semi-discrete formulation of the PDE:

$$\mathbf{M}\dot{\hat{\mathbf{v}}} = -\mathbf{K}\hat{\mathbf{v}} + \hat{\mathbf{I}}^{app}, \quad (22)$$

where the entries of the mass $\mathbf{M}$ and stiffness $\mathbf{K}$ matrices, according to the Einstein notation, are given by:

$$\mathrm{M}_{ab} = \int_\Omega \mathrm{N}_a \mathrm{N}_b\, d\boldsymbol{x}, \quad (23)$$

$$\mathrm{K}_{ab} = \frac{\lambda}{\chi C_m\,(\lambda+1)}\int_\Omega \frac{\partial \mathrm{N}_a}{\partial x_i} d_{ij} \frac{\partial \mathrm{N}_b}{\partial x_j}\, d\boldsymbol{x}, \quad (24)$$

and the entries of the vector $\hat{\mathbf{I}}^{app}$ read as:

$$\hat{\mathrm{I}}_a^{app} = -\frac{1}{\chi C_m\,(\lambda+1)}\int_\Omega \mathrm{N}_a\,(\lambda I_i^{app} - I_e^{app})\, d\boldsymbol{x}. \quad (25)$$

In the numerical computation of these integrals, we employ the standard Gauss quadrature rule with $p+1$ Gauss points in each direction per element, where p is the basis functions degree. Electrophysiological simulations with detailed cellular models may be computationally demanding [25] and to reduce this effort we adopt the Ionic Current Interpolation (ICI) approach, as shown in [23]. In this work, we investigate the effect of the basis function degree and continuity on the accuracy of such an approach.

The ICI method interpolates the ionic current as:

$$I^{ion} = \mathbf{N}(\boldsymbol{x})\,\hat{\mathbf{I}}^{ion}(t). \quad (26)$$

where the components of the vector $\hat{\mathbf{I}}^{ion}$ are computed in terms of control variables:

$$\hat{\mathrm{I}}_a^{ion} = I^{ion}\left(\hat{\mathrm{v}}_a, \hat{\mathrm{w}}_a^1, \dots, \hat{\mathrm{w}}_a^{18}, \hat{\mathrm{c}}_a^1, \hat{\mathrm{c}}_a^2, \hat{\mathrm{c}}_a^3\right), \quad (27)$$

which results from the interpolation of the state variables:

$$\begin{cases} w^r(\boldsymbol{x},t) = \mathbf{N}(\boldsymbol{x})\,\hat{\mathbf{w}}^r(t) & \text{for} \quad r = 1,\dots,18 \quad (28a) \\ c^s(\boldsymbol{x},t) = \mathbf{N}(\boldsymbol{x})\,\hat{\mathbf{c}}^s(t) & \text{for} \quad s = 1,2,3. \quad (28b) \end{cases}$$

Substituting equation (26) in equation (18) and introducing the same approximation of the state variables (28) for their test functions:

$$\begin{cases} \delta w(\boldsymbol{x},t) = \mathbf{N}(\boldsymbol{x})\,\boldsymbol{\delta}\hat{\mathbf{w}}(t) & (29a) \\ \delta c(\boldsymbol{x},t) = \mathbf{N}(\boldsymbol{x})\,\boldsymbol{\delta}\hat{\mathbf{c}}(t), & (29b) \end{cases}$$

a system of ODEs is derived for steps one and three of the Strang scheme, where the components of the control variable vector $\hat{\mathbf{m}}_w^r$ are computed as:

$$(\hat{\mathrm{m}}_w^r)_a = m_w^r\left(\hat{\mathrm{v}}_a, \hat{\mathrm{w}}_a^1, \dots, \hat{\mathrm{w}}_a^{18}\right) \text{ for } r = 1,\dots,18 \quad (30)$$

and similar relations hold for $\hat{\mathbf{m}}_c^s$. Indeed, every entry corresponds to the integration of one control variable, since the mass matrix – on the left and right-hand sides of (18) – is positive definite:

$$\begin{cases} \dot{\hat{\mathbf{v}}} = -\dfrac{1}{C_m}\hat{\mathbf{I}}^{ion} & (31a) \\ \dot{\hat{\mathbf{w}}}^r = \hat{\mathbf{m}}_w^r \qquad \text{for} \quad r = 1,\dots,18 & (31b) \\ \dot{\hat{\mathbf{c}}}^s = \hat{\mathbf{m}}_c^s \qquad \text{for} \quad s = 1,2,3. & (31c) \end{cases}$$

3.4. **Time discretization.** To discretize in time the *Monodomain* formulation, we subdivide the time into equal intervals of size Δt for simplicity, although more refined schemes can be used, since our focus is on spatial discretization. In every time step, we solve the split form of the problem (equations (31) and (22)) using different schemes. Indeed, implicit-explicit schemes are often employed since they guarantee a compromise between numerical stability and computational efficiency, [8].

The non-linear system of ODEs (31) is integrated using the explicit Euler method, with a reduced step size to guarantee sufficient accuracy. Therefore, when considering the sub-step $[t_k, t_{k+1}]$, we adopt the step size $\Delta\tilde{t} = \Delta t/(2k)$:

$$\begin{cases} \hat{\mathbf{v}}_{k+1} = \hat{\mathbf{v}}_k - \dfrac{\Delta\tilde{t}}{C_m}\hat{\mathbf{I}}^{ion}(t_k) & (32a) \\ \hat{\mathbf{w}}_{k+1}^r = \hat{\mathbf{w}}_k^r + \Delta\tilde{t}\,\hat{\mathbf{m}}_w^r(t_k) \quad \text{for} \quad r = 1,\dots,18 & (32b) \\ \hat{\mathbf{c}}_{k+1}^s = \hat{\mathbf{c}}_k^s + \Delta\tilde{t}\,\hat{\mathbf{m}}_c^s(t_k) \quad \text{for} \quad s = 1,2,3. & (32c) \end{cases}$$

In this work, we perform 100 sub-steps (i.e., $k = 100$) during the integration of every reactive step.

In the diffusion step, we use a single increment Δt adopting the implicit, second-order accurate, Crank-Nicolson method to increase the stability of the scheme. The resulting discrete formulation reads as:

$$\left(\mathbf{M} + \frac{\Delta t}{2}\mathbf{K}\right)\hat{\mathbf{v}}_{n+1} = \mathbf{M}\hat{\mathbf{v}}_{k+1} + \frac{\Delta t}{2}\left(-\mathbf{K}\,\hat{\mathbf{v}}_{k+1} + \hat{\mathbf{I}}_n^{app} + \hat{\mathbf{I}}_{n+1}^{app}\right). \quad (33)$$

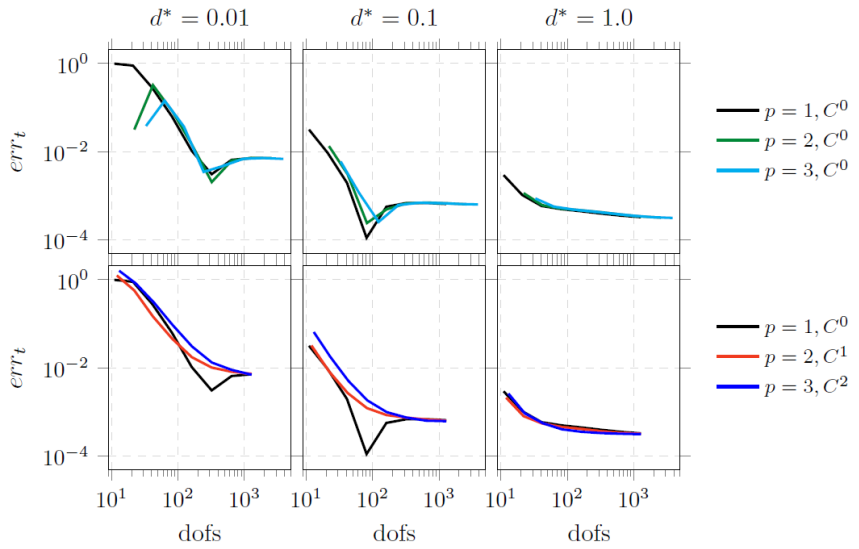

FIGURE 5. Relative errors in the time trace for basis C^0 (top) and C^{p-1} (bottom) basis functions. The black curve, representing linear functions, is repeated in both plot for better comparison.

4. **Numerical simulations.** In this section, we present the results of the electrophysiological simulations performed using the Python-based[1] library Nutils [32]. We assess the proficiency of the presented approach for cultured tissue since, most of the studies in the literature focus on native ones.

The conductivity of the engineered ventricle – characterized by a single scalar value d in 1D rather than a matrix $\mathbf{D}$ – is reduced with respect to the native cardiac tissue, entailing significant implications in the accuracy of the simulation. Indeed, a reduction in the tissue conductivity, for a fixed discretization, results in an increased error in the numerical approximation [33]. Therefore, we first focus on the accuracy in a simple 1D problem: we investigate such a feature limiting the discussion to hiPSC-CMs and varying the normalized conductivity d^*

$$d^* = \frac{\lambda}{\chi C_m \left(\lambda + 1\right)} d \quad \left[\frac{\mathrm{m}^2}{\mathrm{s}}\right]. \tag{34}$$

The Thiele modulus was used to distinguish between reaction-dominated and diffusion-dominated electrophysiological simulations [33] involving several values of conductivity and ionic models. Since we focus on a single-cell model, the Thiele modulus and the normalized conductivity are equivalent definitions up to a constant value.

Based on these results, the 3D model is calibrated and a complete simulation of the action potential propagation in the ventricle is presented. Parameters adopted to perform the simulations are provided in the text, while the initial conditions are provided in Appendix B. Moreover, for the parameters characterizing the cellular model, the reader is referred to [22].

[1]Part of the code will be made available on request.

4.1. **Accuracy investigation.** We investigate the response of a straight fiber (length $L = 3.2$ mm) to assess the effect of different basis function degrees and continuity on the accuracy of the numerical discretization for different values of tissue conductivity. Specifically, we test the basis functions of orders $p = 1, 2, 3$ and continuity $C = 0, p-1$ presented in Section 3.1 for three different values of conductivity $d^* \in \{1.0, 0.1, 0.01\}\,\mathrm{mm}^2/\mathrm{ms}$.

We conduct the convergence analysis under h-refinement simulating a single action potential propagation ($T = 1250$ ms) – triggered by 10 ms of stimulation at the left end ($\boldsymbol{x}^\star = 0$ mm) – using a time step size $\Delta t = 10^{-2}$ ms and an element sizes $h \in \{0.32/(2^k), k = 0, 1, \dots, 7\}$ mm. Since no analytical solution is available, we adopt as a reference v^{ref} an overkill simulation performed using cubic finite elements ($p = 3$, $C = 0$) on a four times finer mesh ($h = 0.32/(2^9)$ mm), and $\Delta t = 10^{-4}$ ms. The results are compared using different metrics.

4.1.1. *Error in the time trace.* We analyze the convergence of the potential in a fixed point of the fiber ($\boldsymbol{x}^\star = 2.7933$ mm, such that the point is never a node) defined as:

$$err_t = \sqrt{\frac{\int_0^T \left(v(\boldsymbol{x}^\star, t) - v^{ref}(\boldsymbol{x}^\star, t)\right)^2 dt}{\int_0^T \left(v^{ref}(\boldsymbol{x}^\star, t)\right)^2 dt}}. \tag{35}$$

The results of the analyses are presented in Figure 5 and discussed as follows.

When the mesh is refined, the error decreases reaching a plateau due to the residual time discretization error, as in [28]. Indeed, a finer time step is adopted in the computation of v^{ref}. Therefore, after a threshold value, both the element size h and the time step size Δt must be refined to improve the accuracy of the solution. Results also highlight that the convergence path depends on the conductivity, confirming that for reaction-dominated simulations the mesh must be finer to retrieve a predefined level of accuracy [33]. The basis function degree and continuity do not affect significantly the accuracy of the solution. Indeed, the error stabilizes approximately for the same number of degrees of freedom (dofs). However, a high continuity (i.e., $C = 1, 2$) provides a monotone convergence path, avoiding the error oscillation before the plateau.

4.1.2. *Error in the spatial representation of the wave.* We analyzed the convergence in a fixed instant $t^\star$, defined as:

$$err_s = \sqrt{\frac{\int_0^L \left(v(\boldsymbol{x}, t^\star) - v^{ref}(\boldsymbol{x}, t^\star)\right)^2 dx}{\int_0^L \left(v^{ref}(\boldsymbol{x}, t^\star)\right)^2 d\boldsymbol{x}}}. \tag{36}$$

In this case, we select different instants for different values of conductivity ($t^\star = 11$ ms for $d^* = 1, 0.1\,\mathrm{mm}^2/\mathrm{ms}$, and $t^\star = 95$ ms for $d^* = 0.01\,\mathrm{mm}^2/\mathrm{ms}$) to avoid the analysis of completely depolarized domains.

Results are presented in Figure 6 and herein discussed.

Differently from the previous analysis, a direct comparison between values of conductivity is no more applicable. Indeed, the temporal shape of an action potential is not affected by the conductivity values up to a temporal shift, while this is not true for the spatial distribution, since the entire impulse is not included in the physical domain. Nevertheless, they confirm the previous findings, suggesting a qualitative independence of the accuracy on the basis function continuity and degree for the analyzed time steps.

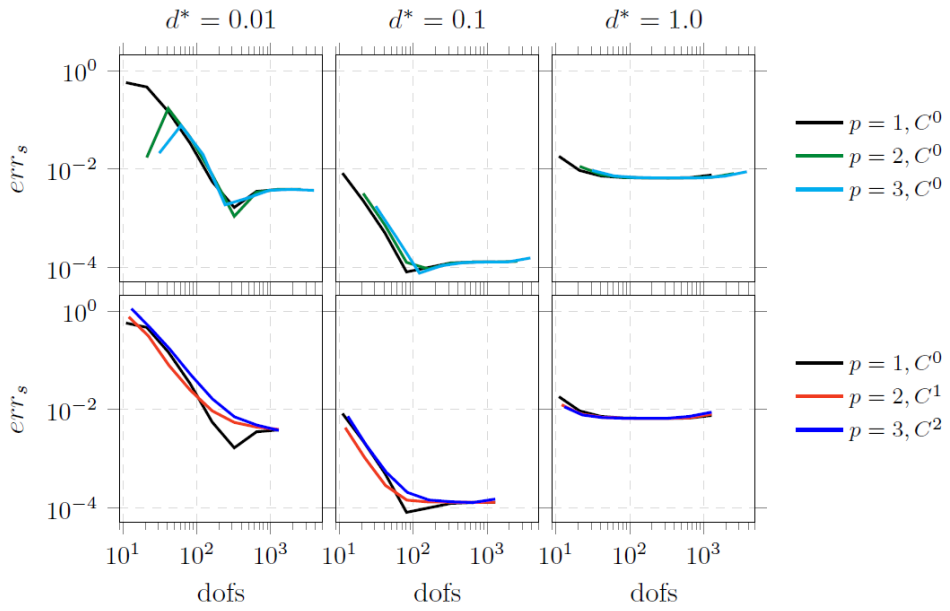

FIGURE 6. Relative errors in spatial representation of the wave for C^0 (top) and C^{p-1} (bottom) basis functions. The black curve, representing linear basis functions, is repeated in both plot for better comparison.

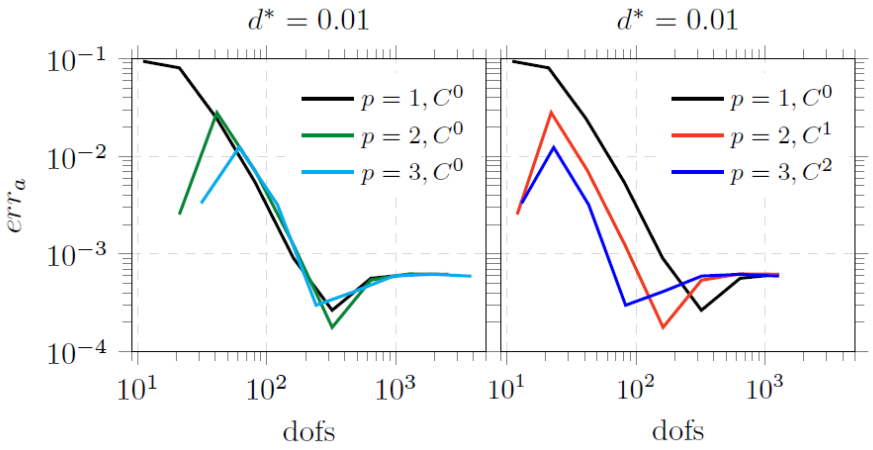

FIGURE 7. Relative errors on arrival time, for C^0 (left) and C^{p-1} (right) basis functions. The black curve, representing linear basis functions, is repeated in both plot for better comparison.

4.1.3. *Error in the wave arrival time.* Having assessed the effect of the conductivity on the accuracy, we specialize our study on the engineered tissue. We further

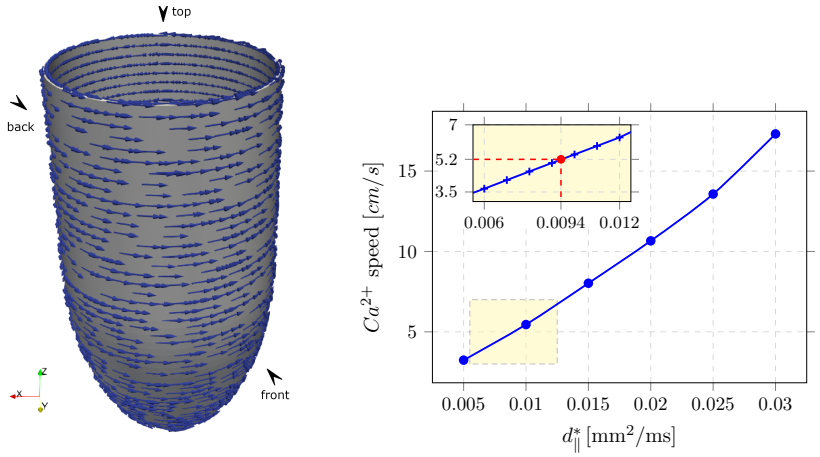

(A) Fibers direction (B) Simulated conduction velocity

FIGURE 8. Calibration of the ventricle model. Fiber direction is represented on the B-spline volume in Figure 8a. The conductivity in the fibers direction is computed as in Figure 8b to reach the desired experimental wave velocity.

investigate the approximation of wave arrival time in $\boldsymbol{x}^\star = 2.7933$ mm, defined as:

$$err_a = \left| \frac{\bar{t} - \bar{t}^{ref}}{\bar{t}^{ref}} \right|, \qquad \text{where} \quad \bar{t} = \arg\max_{t \in [0,T]} \frac{dv(\boldsymbol{x}^\star, t)}{dt} \tag{37}$$

through a forward difference.

In such a definition $\bar{t}^{ref}$ represents the arrival time, computed with the same approach, of the reference solution.

As depicted in Figure 7, we focus only on the conductivity value qualitatively representative of our problem, which we anticipate to be $d^* = 0.01\,\mathrm{mm}^2/\mathrm{ms}$.

In this case, results highlight that the curves related to the high continuity of splines $C = 1, 2$ reach the plateau for a coarser mesh. The highly continuous cubic splines further improve the accuracy with respect to quadratic splines of the same type. However, the gain in accuracy comes at a cost of a denser matrix structure and, therefore, a greater computational effort. Consequently, we adopt quadratic C^1 B-splines for the analysis of the ventricle as they represent a good compromise between accuracy and computational efficiency, producing a stable convergence path in the previous analysis.

We conclude this section by explaining the differences between the results of the error norms. The wave arrival is mainly influenced by the conduction velocity, which in turn is related to the diffusion term, not to the shape of the action potential. Since the spatial derivatives of the basis functions are only involved in the diffusive term, the wave arrival time may be more sensitive to the continuity of the basis functions than other error metrics. Moreover, the dependence of the solution on the ratio between reactive and diffusive terms has already been observed in [33].

4.2. **Electrophysiological simulation of the engineered ventricle.** In the ventricle, cardiomyocytes derived by hiPSCs are arranged in fibers conferring an anisotropic microstructure to the tissue [19]. It results in a speed propagation of

the Ca^{2+} wave in the fiber direction $\mathbf{a}_0$ higher than in the orthogonal directions. The speed of propagation of the Ca^{2+} signal measured in the engineered ventricle using an imaging technique is 5.2 cm/s in the direction from the apex to the base, while, to compute the velocity in the fiber direction, we refer to an additional investigation on *in-vitro* cultured tissues [14]. Indeed, they report the ratio of the velocities for the value of interest of the orientation order parameter [22], which recapitulates the fiber organization in the ventricle. The estimated velocity is equal to 14 cm/s.

To represent this feature, we defined an anisotropic, transversely isotropic, conductivity tensor $\mathbf{D}$, characterized by two different eigenvalues: $d_\parallel$ (multiplicity $m(d_\parallel) = 1$) associated to $\mathbf{a}_0$, and $d_\perp$ (multiplicity $m(d_\perp) = 2$) that spans the space in the orthogonal directions. We assume that fibers are oriented in the pull-spinning direction used to build the scaffold, approximately 5° with respect to the XY plane, as shown in Figures 8a and 11.

Since the conductivity values are unknown, a calibration to fit the experimental wave velocity is needed: we compute the conductivity for every principal direction d_j^* by constructing a response curve, shown in Figure 8b. The ionic model is unaffected by this process. We simulate 50 s of isotropic action potential propagation ($\Delta t =$ 0.01 ms) in a flat strip (12.1×0.02 mm, $h = 0.01$ mm, $p = 2, C = 1$) computing the average Ca^{2+} speed for different conductivity values. The conductivities in the two orthogonal directions are then obtained by interpolation of the discrete response curve substituting d^* with $d_j = d_\parallel$ or $d_j = d_\perp$ in equation (34).

The conductivity calibration results in the following coefficients of the conductivity tensor: $d_\parallel^* = 0.0094$ and $d_\perp^* = 0.0256$ mm^2/ms. Clearly, more sophisticated procedures are available in the literature [34, 3, 1, 2]. However, they require complete sets of imaging data in space and time to solve the inverse problem, which is out of the scope of this work.

Once the computational framework to simulate the electrophysiological activity of the engineered ventricle is completed, we perform the simulation of an action potential propagation ($T = 1250$ ms, $\Delta t = 0.01$ ms) on the ellipsoidal geometry using a mesh composed by 756012 quadratic C^1 B-splines.

The tissue is stimulated using an applied current ($I_i^{app} = 20$ pA) for 100 ms spatially distributed near $\boldsymbol{x} = (0, 4.5, 2)$ mm to mimic the electrode used in the experimental protocol. The initially repolarized membrane ($v = -74.9$ mV) undergoes an action potential that propagates from the stimulation site toward the rest of the tissue before the spontaneous firing activity of the cells.

The elongated shape of the wave (for instance: v at time $t = 0.2$ s, plot (a)) confirms the faster propagation in the fiber direction. Moreover, the simulation reveals a smooth wavefront, for both the transmembrane potential and the intercellular Ca^{2+}, as shown in Figure 9. Finally, the opposite wavefronts correctly merge on the posterior side of the ventricle, confirming the reliability of the proposed approach and the possibility of conducting trial-and-error investigations on the *in-silico* replica of the ventricle.

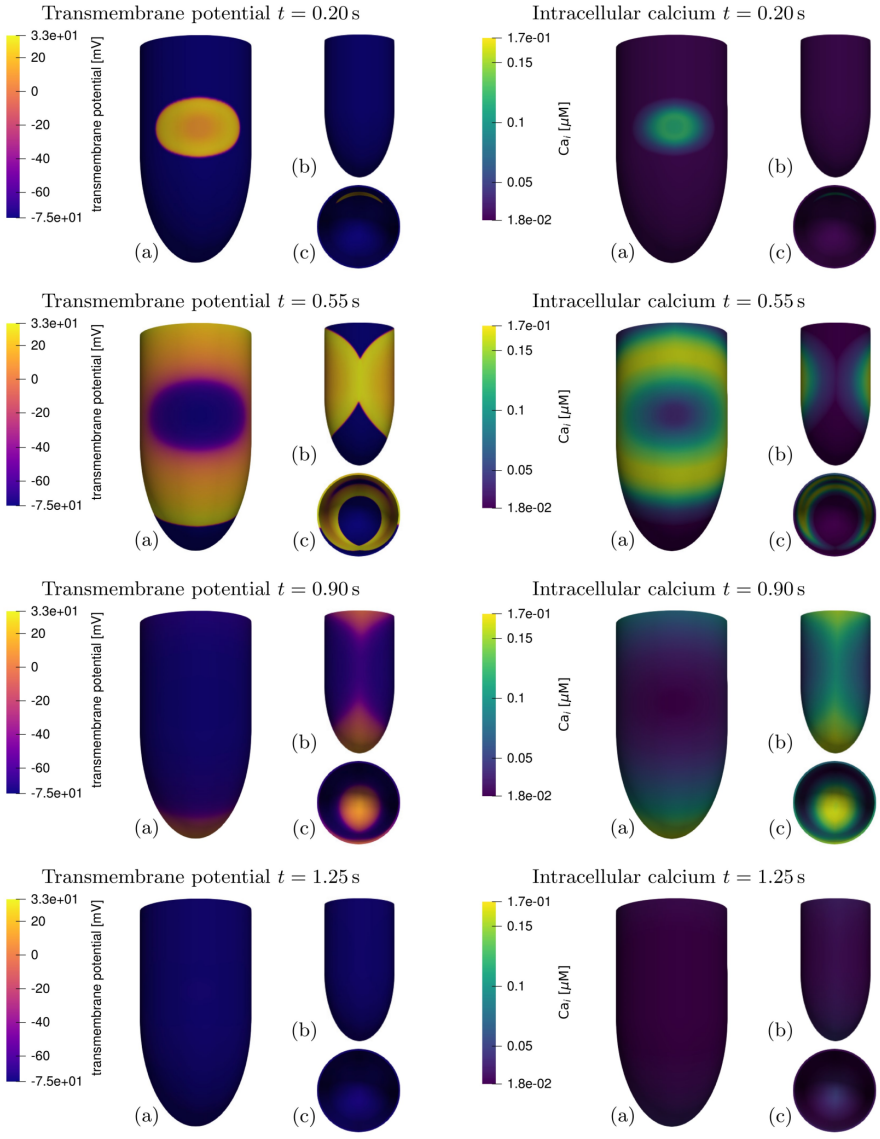

FIGURE 9. Simulation of the engineering ventricle. Representation of the transmembrane potential (on the left) and intracellular Ca^{2+} concentration (on the right) on the front (a), back (b), and top (c) views (see Figure 8a) for representative time steps.

5. **Conclusions and future perspectives.** In this work, we have developed a computational framework useful to investigate the electrophysiological response of the engineered ventricle [19]. To model the tissue, we have included an advanced ionic model [22], tailored for hiPSC-CMs, into the *Monodomain* formulation. Furthermore, we have reproduced the fibrous structure of the construct using an anisotropic conductivity tensor with principal directions variable over the ellipsoidal geometry.

The mathematical formulation is discretized, in the spirit of a Galerkin method, using several sets of B-splines. Differently from previous investigations [23, 5], we are not approaching the human adult tissue, but we focused on a novel regenerative medicine frontier based on hiPSC-CMs technology, which entails different numerical issues. We have assessed the dependence of the discretization accuracy on the basis function degree and continuity, using several metrics to define the error. Based on our findings, quadratic C^1 B-splines are a good compromise between accuracy and computational effort. Such an isogeometric framework was then employed in the calibration of the numerical model and in the simulation of the propagation of an action potential in the engineered ventricle.

In summary, our results demonstrate that innovative stem cell tissues and organoids can be properly represented *in-silico*, with implications for regenerative medicine research. Since hiPSC-CMs have the same genetic heritage of the donor, this may extend patient-specific assays from individual cells to complete organ models. Specifically, our computational framework enables fast parametric investigation when considering different scenarios depending on the patient-specific conditions. Conversely, laboratory tests require a higher number of ventricle replications to guarantee a significant statistical sample entailing a great economic effort.

Once more, maturation studies provide innovative pools of hiPSC-CMs in the direction of a more adult phenotype. Since the *in-silico* framework reveals the possibility of disentangling the ionic model from tissue properties, we offer a tool to simulate the variation of the physiological response due to the maturation process, considering several ionic models for different maturation states.

Furthermore, investigations could aim to model a more complex experimental setup, such as a hole in the virtual geometry using an immersed technology [29]. Investigations on injured tissue, considering a single-hole injury or a hole pair, may provide a better understanding of complex pathological phenomena, for instance, the formation of spiral waves. In such a context, the non-homogeneous distribution of the tissue properties should be considered in the future to assess their effect in pathological conditions.

This work only considers cardiac electrophysiological simulations, neglecting tissue contraction. Mechanics could also be included, as shown in [20], further improving the realism of the simulation. Indeed, the *in-vitro* setup also investigates the intraventricular pressure-volume loops using catheter-based systems to assess the effect of compounds on tissue contractility.

Acknowledgments. MT gratefully acknowledges the financial support of the Italian Ministry for Education, University and Research (MIUR) through the PRIN project XFAST-SIMS (no. 20173C478N to Alessandro Reali) and the contribution of the National Recovery and Resilience Plan, Mission 4 Component 2 – Investment 1.4 – CN_00000013 CENTRO NAZIONALE "HPC, BIG DATA E QUANTUM COMPUTING", spoke 6. SB was supported by grants of Istituto Nazionale di Alta Matematica (INDAM-GNCS).

Appendix A. **Mapping procedure for unstructured surfaces.** In this section, we present an alternative algorithm to map a surface, provided through a stereolithography file, using a B-spline manifold. Indeed, if the analytical formulation describing the surface is unknown, the definition of the relation that associates the points on the spline surface to the points on the real surface may be a complex task.

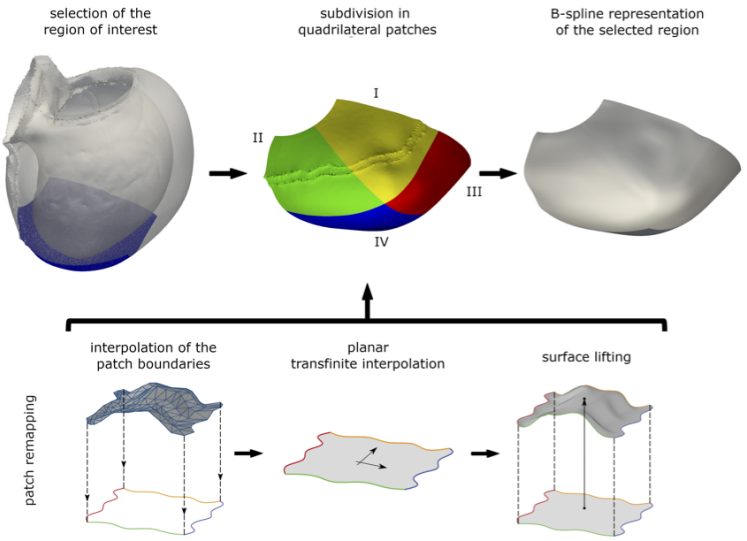

FIGURE 10. Mapping procedure for faceted surfaces.

The procedure involves several steps, as shown in Fig. 10. For illustration purposes, we apply the methodology to remap a portion of the apex of a real human left ventricle although it is not used in the present work.

- The first step subdivides the faceted surface into patches, requiring that every point in the patch can be projected on a predefined plane without intersecting the patch surface, clearly the choice of the plane can vary from patch to patch.
- Once the surface is subdivided in patches, we interpolate the flat projection of the 4 boundaries – subdivided using 4 user-defined points – using 2 sets of B-splines, adopting the same degree and knot vector on opposite edges.
- Given the planar interpolation of the 4 edges, we fill the flat spline surface by means of transfinite interpolation of the control point coordinates, as described in [10].
- The third coordinate, the elevation, of the points representing the manifold is retrieved by means of L_2 projection, avoiding the definition of the ordering of the points. Indeed, the parametric coordinates of a point are mapped into the planar B-spline surface and then elevated interpolating the nodes coordinates of the original facet.
- Given the geometrical mapping of every patch, either we can use a multipatch geometry or we can remap the surface into a single patch by means of L_2 approximation if the patch union constitutes a rectangle in the parametric space.

Appendix B. **Computational details.** The first version of the Paci ionic model is available from the CellML repository (`http://models.cellml.org/cellml`) and the updated set of equations and the complete list of parameters are presented in the online Supplementary Material of [22].

The magnitude of the applied current is $\lambda I_i^{app} - I_e^{app} = 20\,\text{pA}$, and the initial conditions are computed simulating 800s of spontaneous activity of a single cell,

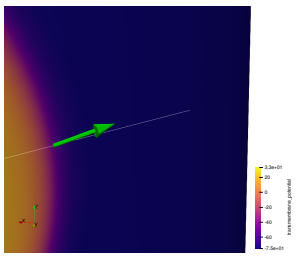

FIGURE 11. Zoom on the front of the fiber orientation: in green the direction $\mathbf{a}_0$ and in white a reference line (tangent to the scaffold and lying in a plane parallel to the XY plane).

starting from the conditions reported in [22], to ensure steady-state conditions. They are summarized, according to the notation in [22], in Table 1.

Variables	Units	Values
V_0	V	-0.0749
Ca_{SR}	mM	0.0937
Ca_i	mM	3.7968e-05
d_0	-	8.2522e-05
$f1_0$	-	0.7411
$f2_0$	-	1.0000
fCa_0	-	0.9977
$Xr1_0$	-	0.2661
$Xr2_0$	-	0.4349
Xs_0	-	0.0314
h_0	-	0.7454
j_0	-	0.0761
m_0	-	0.0996
Xf_0	-	0.0249
q_0	-	0.8417
r_0	-	0.0056
Na_i	mM	8.6482
mL_0	-	0.0023
hL_0	-	0.0812
$RyRa_0$	-	0.0387
$RyRo_0$	-	0.0260
$RyRc_0$	-	0.0786

TABLE 1. Initial conditions

To better highlight the fiber orientation, in Figure 11 we zoom a portion of the wave front at coordinates $(-3.28, 3.37, 2.34)$ mm with respect to the frame placed in the center of the half-ellipsoid. Specifically, the contour plot of the transmembrane potential at time t=0.2 s (see Figure 9) is represented.

REFERENCES

[1] A. Barone, M. G. Carlino, A. Gizzi, S. Perotto and A. Veneziani, Efficient estimation of cardiac conductivities: A proper generalized decomposition approach, *J. Comput. Phys.*, **423** (2020), 109810.

[2] A. Barone, A. Gizzi, F. Fenton, S. Filippi and A. Veneziani, Experimental validation of a variational data assimilation procedure for estimating space-dependent cardiac conductivities, *Comput. Meth. Appl. Mech. Eng.*, **358** (2020), 112615.

[3] A. Barone, F. Fenton and A. Veneziani, Numerical sensitivity analysis of a variational data assimilation procedure for cardiac conductivities, *Chaos*, **27** (2017), 093930.

[4] S. Botti, *Mathematical Modeling of Human Induced Pluripotent Stem Cell-Derived Cardiomyocytes (hiPSC-CMs): From Ionic Currents to 3D Ventricle Models*, Ph.D thesis, University of Pavia, Italy, 2022.

[5] M. Bucelli, M. Salvador, L. Dedè and A. Quarteroni, Multipatch Isogeometric Analysis for electrophysiology: Simulation in a human heart, *Comput. Meth. Appl. Mech. Eng.*, **376** (2021), 113666.

[6] J. A. Cottrell, T. J. R. Hughes and Y. Bazilevs, *Isogeometric Analysis: Toward Integration of CAD and FEA*, 1^{st} edition, John Wiley & Sons, 2009.

[7] A. Eder, I. Vollert, A. Hansen and T. Eschenhagen, Human engineered heart tissue as a model system for drug testing, *Advan. Drug Deliv. Rev.*, **96** (2016), 214-224.

[8] P. C. Franzone, L. F. Pavarino and S. Scacchi, *Mathematical Cardiac Electrophysiology*, 1^{st} edition, Springer, 2014.

[9] I. Goldfracht, Y. Efraim, R. Shinnawi, E. Kovalev, I. Huber, A. Gepstein, G. Arbel, N. Shaheen, M. Tiburcy , W. H. Zimmermann, M. Machluf and L. Gepstein, Engineered heart tissue models from hiPSC-derived cardiomyocytes and cardiac ECM for disease modeling and drug testing applications, *Acta Biomat.*, **92** (2019), 145-159.

[10] W. J. Gordon and L. C. Thiel, Transfinite mappings and their application to grid generation, *Appl. Math. Comput.*, **10** (1982), 171-233.

[11] J. P. Keener and J. Sneyd, *Mathematical Physiology*, 1^{st} edition, Springer, 1998.

[12] J. Kiendl, *Isogeometric Analysis and Shape Optimal Design of Shell Structures*, Ph. D thesis, Technische Universität München, Germany, 2011.

[13] J. T. Koivumäki, T. Korhonen and P. Tavi, Impact of sarcoplasmic reticulum calcium release on calcium dynamics and action potential morphology in human Atrial myocytes: A computational study, *PLoS Comput. Biol.*, **7** (2011), e1001067.

[14] J. U. Lind, A. Busbee, A. D. Valentine, F. S. Pasqualini, H. Yuan, M. Yadid, S. Park, A. Kotikian, A. P. Nesmith, P. H. Campbell, J. J. Vlassak, J. A. Lewis and K. K. Parker, Instrumented cardiac microphysiological devices via multimaterial three-dimensional printing, *Nature Mater.*, **16** (2017), 303-308.

[15] A. M. Lodrini, L. Barile, M. Rocchetti and C. Altomare, Human induced pluripotent stem cells derived from a cardiac somatic source: Insights for an in-vitro cardiomyocyte platform, *Int. J. Molec. Sci.*, **21** (2020).

[16] A. Lopez-Perez, R. Sebastian, M. Izquierdo, R. Ruiz, Ricardo, M. Bishop and J. M. Ferrero, Personalized cardiac computational models: From clinical data to simulation of infarct-related ventricular tachycardia, *Front. Physiol.*, **10** (2019).

[17] S. D. Lundy, W. Zhu, M. Regnier and M. A. Laflamme, Structural and functional maturation of cardiomyocytes derived from human pluripotent stem cells, *Stem Cells Devel.*, **22** (2013), 1991-2002.

[18] L. A. MacQueen, S. P. Sheehy, C. O. Chantre, J. F. Zimmerman, F. S. Pasqualini, X. Liu, J. A. Goss, P. H. Campbell, G. M. Gonzalez, S. Park, A. K. Capulli, J. P. Ferrier, T. F. Kosar, L. Mahadevan, W. T. Pu and K. K. Parker, Addendum: A tissue-engineered scale model of the heart ventricle, *Nature Biomed. Eng.*, 2022.

[19] L. A. MacQueen, S. P. Sheehy, C. O. Chantre, J. F. Zimmerman, F. S. Pasqualini, X. Liu, J. A. Goss, P. H. Campbell, G. M. Gonzalez, S. Park, A. K. Capulli, J. P. Ferrier, T. F. Kosar, L. Mahadevan, W. T. Pu and K. K. Parker, A tissue-engineered scale model of the heart ventricle, *Nat. Biomed. Eng.*, **12** (2018), 930-941.

[20] A. Nitti, J. Kiendl, A. Gizzi, A. Reali and M. D. de Tullio, A curvilinear isogeometric framework for the electromechanical activation of thin muscular tissues, *Comput. Meth. Appl. Mech. Eng.*, **382** (2021), 113877.

[21] M. Paci, J. Hyttinen, K. Aalto-Setälä and S. Severi, Computational models of ventricular- and atrial-like human induced pluripotent stem cell derived cardiomyocytes, *Ann. Biomed. Eng.*, **41** (2013), 2334-2348.
[22] M. Paci, R. Pölönen, D. Cori, K. Penttinen, K. Aalto-Setälä, S. Severi and J. Hyttinen, Automatic optimization of an in silico model of human iPSC derived cardiomyocytes recapitulating calcium handling abnormalities, *Front. Physiol.*, **9** (2018), 709.
[23] A. S. Patelli, L. Dedè, T. Lassila, A. Bartezzaghi and A. Quarteroni, Isogeometric approximation of cardiac electrophysiology models on surfaces: An accuracy study with application to the human left atrium, *Comput. Meth. Appl. Mech. Eng.*, **317** (2017), 248-273.
[24] A. Santiago, J. Aguado-Sierra, M. Zavala-Aké, R. Doste-Beltran, S. Gómez, R. Arís, J. C. Cajas, E. Casoni and M. Vázquez, Fully coupled fluid-electro-mechanical model of the human heart for supercomputers, *Inter. J. Numer. Meth. Biomed. Eng.*, **34** (2018), e3140.
[25] J. Sundnes, G. T. Lines, X. Cai, B. F. Nielsen, K. Mardal and A. Tveito, *Computing the Electrical Activity in the Heart*, 1^{st} edition, Springer Science & Business Media, 2007.
[26] K. Takahashi, K. Tanabe, M. Ohnuki, M. Narita, T. Ichisaka, K. Tomoda and S. Yamanaka, Induction of pluripotent stem cells from adult human fibroblasts by defined factors, *Cell*, **131** (2007), 861-872.
[27] K. Takahashi and S. Yamanaka, Induction of pluripotent stem cells from mouse embryonic and adult fibroblast cultures by defined factors, *Cell*, **126** (2006), 663-676.
[28] M. Torre, S. Morganti, A. Nitti, M. D. de Tullio, F. S. Pasqualini and A. Reali, An efficient isogeometric collocation approach to cardiac electrophysiology, *Comput. Meth. Appl. Mech. Eng.*, **393** (2022), 114782.
[29] M. Torre, S. Morganti, F. S. Pasqualini, A. Düster and A. Reali, Immersed isogeometric analysis based on a hybrid collocation/finite cell method, *Comput. Meth. Appl. Mech. Eng.*, **405** (2023), 115856.
[30] N. A. Trayanova and R. Winslow, Whole-Heart Modeling, *Circ. Res.*, **108** (2011), 113-128.
[31] E. Tzatzalos, O. J. Abilez, P. Shukla and J. C. Wu, Engineered heart tissues and induced pluripotent stem cells: Macro- and microstructures for disease modeling, drug screening, and translational studies, *Advan. Drug Deliv. Rev.*, **96** (2016), 234-244.
[32] G. van Zwieten , J. van Zwieten and W. Hoitinga *Nutils 7.0 Zenodo*, Available from: `https://doi.org/10.5281/zenodo.6006701`.
[33] K. P. Vincent, M. J. Gonzales, A. K. Gillette, C. T. Villongco, S. Pezzuto, J. H. Omens, M. J. Holst and A. D. McCulloch, High-order finite element methods for cardiac monodomain simulations, *Front. Physiol.*, **6** (2015), 217.
[34] H. Yang and A. Veneziani, Efficient estimation of cardiac conductivities via POD-DEIM model order reduction, *Appl. Numer. Math.*, **115** (2017), 180-199.

Received March 2023; revised August 2023; early access August 2023.